Research Article

Yanfeng Yang*, Chaolin Liu, and Feng Xin

Numerical investigation of acoustic streaming vortices in cylindrical tube arrays

https://doi.org/10.1515/phys-2024-0022
received November 25, 2023; accepted April 17, 2024

Abstract: Acoustic streaming has a significant effect on accelerating material mixing and flow field disturbance. To explore the characteristics of acoustic streaming in the cylindrical tube array field under the action of an acoustic wave, we derive the dimensionless acoustic streaming control equation and establish a numerical calculation model of acoustic streaming. The effects of acoustic incidence angle, acoustic Reynolds number, and Strouhal number on the acoustic streaming vortex flow field in the tube array were investigated. The numerical results show that with the change in acoustic parameters, the acoustic streaming in the tube array presents rich changes in the vortex flow field, and there are flow field phenomena such as shrinking, merging, tearing, and splitting of the vortex structure. Toward the walls of each tube, there is a strong acoustic streaming flow velocity. Besides, there is also a large streaming velocity on the interface of the adjacent acoustic streaming vortices. The inner streaming vortex structure in the acoustic boundary layer decreases with the increase in the acoustic Reynolds number, but the intensity of the inner streaming vortex and outer streaming vortex increases rapidly, and the disturbance effect of the flow field is enhanced. With the increase in the dimensionless acoustic frequency (or Strouhal number), although the structure and intensity of the inner streaming vortex decrease, the velocity gradient on the wall of the cylindrical tube increases, which is beneficial to destroy the flow boundary layer of the cylindrical tube wall and accelerate the instability of the wall flow field.

Keywords: tube arrays, acoustic streaming, vortex, acoustic Reynolds number

*** Corresponding author: Yanfeng Yang,** College of Energy and Power Engineering, Changsha University of Science and Technology, Changsha 410114, China; Hebei Key Laboratory of Physics and Energy Technology, Baoding 071003, China, e-mail: yfyang2022@csust.edu.cn
Chaolin Liu, Feng Xin: College of Energy and Power Engineering, Changsha University of Science and Technology, Changsha 410114, China

1 Introduction

In recent years, sound waves have been widely used and studied in power plant boilers [1,2]. For example, strong sound waves can not only clean the ash accumulation on the pipe wall but also destroy the boundary layer structure, thereby reducing the thermal resistance of heat exchange and improving the heat exchange efficiency of the heat exchanger [3,4]. It is worth noting that the acoustic streaming effect formed by sound waves around the heat exchanger tube is an important mechanism for improving the heat exchange efficiency [5]. By interacting with obstacles, strong sound waves create acoustic streaming, which is an important nonlinear acoustic phenomenon [6]. The vortex effect of the acoustic streaming can accelerate the mixing and heat transfer process of the materials [7–9]. Given the advantages of the acoustic streaming effect, many researchers have studied the acoustic streaming motion based on simple geometric models, such as the two-dimensional closed channel model [10,11], two-dimensional sphere [12,13], and cylinder model [14,15]. However, the evolution law of the acoustic streaming flow field in the periodic tube array structure field needs to be studied in detail.

The vibration of an object immersed in a viscous fluid will also produce steady streaming [16], and its mechanism is similar to that of acoustic streaming. For example, Bahrani *et al.* [15] experimentally studied the steady streaming phenomenon caused by the high amplitude forced oscillation of a cylinder in a viscous fluid and discussed the effects of different frequencies and amplitudes on the scale and intensity of vortices inside and outside the acoustic boundary layer. Nuriev *et al.* [14] directly and numerically studied the steady streaming induced by a vibrating cylinder with different dimensionless amplitudes and vibration acoustic Reynolds numbers. The results show that steady streaming has various structures and characteristics within the range of control parameters. Yong [17] proposed a series solution method for solving the potential field and stokes flow and studied the steady streaming induced by the self-excited vibration of two linearly arranged cylinders. It is found that the steady

streaming around the cylinder is a rich flow pattern structure with the change in cylinder spacing and vibration direction. Yan *et al.* [18] numerically and experimentally studied the problem of steady streaming caused by harmonic vibration of single-row parallel cylindrical tube bundles in a viscous fluid. The results show that for the low acoustic Reynolds number, there are four symmetrical acoustic streaming vortices around each cylinder. However, when the acoustic Reynolds number is large, the symmetry of the vortex is destroyed. Coenen [19] experimentally and numerically studied the steady streaming motion around a pair of circular cylinders placed in a small amplitude oscillatory flow. The effects of intercolumn gap width and acoustic Reynolds number on the flow topology are studied. Valverde [7,20] numerically calculated the evolution of acoustic streaming when sound waves acted on an array of microscale cylindrical tubes in the presence of a background flow field. The flow structure of acoustic streaming presents rich flow patterns with the change in background velocity. An *et al.* [21] numerically studied the steady streaming formed around a cylinder under the action of oscillating flow. It is found that the characteristics of steady streaming are closely related to the flow state of vortex shedding. Chini *et al.* [22] studied the flow field characteristics of large-amplitude acoustic streaming and found that the velocity of acoustic streaming was equivalent to the instantaneous velocity of fluid particles induced by the sound field. In this case, the formation mechanism of acoustic streaming had nothing to do with fluid viscosity but was related to the fluctuating baroclinic torques caused by large amplitude acoustic waves. The above studies are all from the perspective of fluid mechanics to study the characteristics of the time-average flow field, without considering the influence of a non-uniform temperature field on acoustic streaming. It can be imagined that the study of practical physical problems often involves a temperature field. Based on the Navier–Stokes compressible equation, ideal gas model, and finite volume discretization, Malecha [23] conducted a three-dimensional numerical study on the acoustic streaming phenomenon in a rectangular resonator with a 60 K temperature difference between the upper and lower walls. It is found that the sound flow driven by large amplitude acoustic waves is stronger in non-isothermal flow than in isothermal flow. The change in fluid density caused by a non-uniform temperature field is the key to the change in acoustic streaming intensity and vortex scale [24].

In summary, many researchers have comprehensively studied the steady streaming phenomenon induced by the self-excited oscillation of single-cylinder and single-row cylindrical arrays in a viscous fluid. However, the acoustic streaming in the structural field of multi-row cylindrical tube arrays under the action of strong sound waves has not been studied in detail. The structure of the study is as follows: in Section 2, the dimensionless time-averaged acoustic streaming control equation is derived in detail, which explains theoretically that the sound flow motion is driven by Reynolds stress. In Section 3, the numerical calculation model of acoustic streaming in a tube array is introduced, and the numerical calculation steps are given. In Section 4, the acoustic incidence angle, acoustic Reynolds number, and Strouhal number on the acoustic streaming vortex in the tube array are discussed in detail. Section 5 summarizes the main conclusions of the study.

2 Governing equations

The governing equation of fluid motion induced by sound wave is as follows [22,25]:

$$\rho\left[\frac{\partial \boldsymbol{u}}{\partial t} + (\boldsymbol{u}\cdot\nabla)\boldsymbol{u}\right] = -\nabla p + \left(\mu_{\mathrm{B}} + \frac{1}{3}\mu\right)\nabla(\nabla\cdot\boldsymbol{u}) + \mu\nabla^2\boldsymbol{u}, \tag{1a}$$

$$\frac{\partial \rho}{\partial t} + \nabla\cdot(\rho\boldsymbol{u}) = 0, \tag{1b}$$

$$\rho c_v\left[\frac{\partial T}{\partial t} + (\boldsymbol{u}\cdot\nabla)T\right] = -p(\nabla\cdot\boldsymbol{u}) + k\nabla^2 T + Q, \tag{1c}$$

where $\boldsymbol{u}$ is the fluid velocity, p is the fluid pressure, ρ is the fluid density, μ is the dynamic fluid viscosity, and μ_{B} is the volume fluid viscosity. t is the time, c_{v} is the specific heat coefficients at constant volume, k is the thermal conductivity, T is the medium temperature, Q is the extra heat source ($Q = 0$). In this work, the effect of non-uniform temperature field on acoustic streaming induced by sound wave is not considered, and the heat loss of sound wave is ignored. Because of the heat loss caused by the interaction between the sound field and the wall leads to little change in the fluid temperature [26], Eq. (1c) is not considered in the numerical solution.

Eqs. (1a) and (1b) need to be combined with equations of state to become closed systems. The calculated medium is approximated as an ideal gas, satisfying the following relation [13]:

$$p - p_0 = c^2(\rho - \rho_0), \tag{2}$$

where c is the speed of sound, which is related to the medium temperature, and the temperature in the calculation domain is set to be uniform, so the sound speed is constant. And p_0 and ρ_0 are the equilibrium fluid pressure and density, respectively.

To consider the generality of physical problems, it is appropriate to transform Eqs. (1a) and (1b) into

dimensionless equations. After dimensionless treatment of the physical quantities in Eqs. (1) and (2), the relations are as follows:

$$\begin{aligned} &\boldsymbol{u}^* = \boldsymbol{u}/U_0, \quad p^* = p/\rho_0 U_0^2, \quad \tau = U_0 t/H, \\ &\rho^* = \rho/\rho_0, \quad (X, Y) = (x, y)/H, \end{aligned} \tag{3}$$

where H is the height of the inlet of the calculated domain, and U_0 is the amplitude of inlet acoustic velocity.

By substituting Eq. (3) in Eqs. (1a) and (1b), the dimensionless momentum equation and mass equation describing fluid motion can be obtained.

$$\begin{aligned} &\rho^*\left[\frac{\partial \boldsymbol{u}^*}{\partial \tau} + (\boldsymbol{u}^* \cdot \nabla)\boldsymbol{u}^*\right] \\ &\quad = -Lp^* + \left(\frac{1}{\mathrm{Re_B}} + \frac{1}{3\,\mathrm{Re}}\right)L(L \cdot \boldsymbol{u}^*) + \frac{1}{\mathrm{Re}}L^2\boldsymbol{u}^*, \end{aligned} \tag{4}$$

$$\frac{\partial \rho^*}{\partial \tau} + L \cdot (\rho^* \boldsymbol{u}^*) = 0, \tag{5}$$

where $L = H\nabla$, ∇ is the Hamilton operator. Re is the acoustic Reynolds number, $\mathrm{Re} = \rho_0 U_0 H/\mu$. And $\mathrm{Re_B} = \rho_0 U_0 H/\mu_\mathrm{B}$.

We employ Nyborg's perturbation technique [25], and the dimensionless pressure p^*, dimensionless velocity $\boldsymbol{u}^*$, and dimensionless density ρ^* in Eqs. (4) and (5) can be expanded into the following forms:

$$p^* = p_0^* + \varepsilon p_1^* + \varepsilon^2 p_2^* + O(\varepsilon^3) + \cdots, \tag{6a}$$

$$\boldsymbol{u}^* = \boldsymbol{u}_0^* + \varepsilon \boldsymbol{u}_1^* + \varepsilon^2 \boldsymbol{u}_2^* + O(\varepsilon^3) + \cdots, \tag{6b}$$

$$\rho^* = \rho_0^* + \varepsilon \rho_1^* + \varepsilon^2 \rho_2^* + O(\varepsilon^3) + \cdots, \tag{6c}$$

where ε is defined as the ratio of acoustic particle velocity amplitude to local sound speed [27]. The magnitude of ε represents the nonlinear intensity of sound waves. The first-order quantity represents the variables of the acoustical physical field formed in the computational domain under the excitation of boundary conditions. The second-order quantity represents the nonlinear acoustic streaming flow field formed by sound waves in the tube array. If the background flow field is not taken into account, the zero-order velocity $u_0^* = 0$.

By substituting Eqs. (6a)–(6c) in Eqs. (4) and (5), and retaining only the term containing the first power of parameter ε, the following equation can be obtained:

$$\rho_0^* \frac{\partial \boldsymbol{u}_1^*}{\partial \tau} = -Lp_1^* + \left(\frac{1}{\mathrm{Re_B}} + \frac{1}{3\,\mathrm{Re}}\right)L(L \cdot \boldsymbol{u}_1^*) + \frac{1}{\mathrm{Re}}L^2\boldsymbol{u}_1^*, \tag{7}$$

$$\frac{\partial \rho_1^*}{\partial \tau} + \rho_0^* L \cdot \boldsymbol{u}_1^* = 0. \tag{8}$$

Eqs. (7) and (8) describe the relationship between the first-order physical quantities of sound field.

Similarly, substituting Eqs. (6a)–(6c) in Eqs. (4) and (5), and retaining only the term containing the parameter ε quadratic power, the following equation can be obtained:

$$\begin{aligned} &-Lp_2^* + \left(\frac{1}{\mathrm{Re_B}} + \frac{1}{3\,\mathrm{Re}}\right)L(L \cdot \boldsymbol{u}_2^*) + \frac{1}{\mathrm{Re}}L^2\boldsymbol{u}_2^* \\ &\quad = \rho_0^* \frac{\partial \boldsymbol{u}_2^*}{\partial \tau} + \rho_1^* \frac{\partial \boldsymbol{u}_1^*}{\partial \tau} + \rho_0^*(\boldsymbol{u}_1^* \cdot L)\boldsymbol{u}_1^*, \end{aligned} \tag{9}$$

$$\frac{\partial \rho_2^*}{\partial \tau} + \rho_0^* L \cdot \boldsymbol{u}_2^* = -L \cdot (\boldsymbol{u}_1^* \rho_1^*). \tag{10}$$

Furthermore, taking the time average of Eqs. (9) and (10) in one oscillation period can get the following form:

$$\begin{aligned} &-L\langle p_2^* \rangle + \left(\frac{1}{\mathrm{Re_B}} + \frac{1}{3\,\mathrm{Re}}\right)L(L \cdot \langle \boldsymbol{u}_2^* \rangle) + \frac{1}{\mathrm{Re}}L^2\langle \boldsymbol{u}_2^* \rangle \\ &\quad = \left\langle \rho_1^* \frac{\partial \boldsymbol{u}_1^*}{\partial \tau} \right\rangle + \rho_0^* \langle (\boldsymbol{u}_1^* \cdot L)\boldsymbol{u}_1^* \rangle, \end{aligned} \tag{11}$$

$$\rho_0^* L \cdot \langle \boldsymbol{u}_2^* \rangle = -L \cdot \langle \boldsymbol{u}_1^* \rho_1^* \rangle, \tag{12}$$

where $\langle x \rangle$ represents the time average processing of the physical quantity x in one cycle. It can be seen from Eqs. (11) and (12) that the acoustic streaming motion is generated by the nonlinearity of the first-order acoustic field.

The time average is taken after multiplying the Eq. (8) by $\boldsymbol{u}_1^*$, and then substituted in Eq. (11) to obtain

$$\begin{aligned} &-L\langle p_2^* \rangle + \left(\frac{1}{\mathrm{Re_B}} + \frac{1}{3\,\mathrm{Re}}\right)L(L \cdot \langle \boldsymbol{u}_2^* \rangle) + \frac{1}{\mathrm{Re}}L^2\langle \boldsymbol{u}_2^* \rangle \\ &\quad = \rho_0^* L \cdot \langle \boldsymbol{u}_1^* \boldsymbol{u}_1^* \rangle. \end{aligned} \tag{13}$$

The expression to the right of the equal sign of Eq. (13) is called Reynolds stress, which is defined as follows:

$$\boldsymbol{F}_\mathrm{R} = -\rho_0 L \cdot \langle \boldsymbol{u}_1^* \boldsymbol{u}_1^* \rangle. \tag{14}$$

It can be seen from Eq. (14) that the acoustic streaming motion is driven by Reynolds stress. Therefore, the method of simulating acoustic streaming by solving Eq. (14) is called the Reynolds stress method [28]. And we write the corresponding code to calculate the Eqs. (11) and (12) by using the weak form method of the partial differential equation.

3 Numerical study

3.1 Computational model

Figure 1 shows the structural diagram of the cylindrical tube array.

The outer diameter of the cylindrical tube is 38.1 mm, and the longitudinal pitch S_1 and transverse pitch S_2 in the

tube array are both twice the diameter of the cylindrical tube, which is $S_1 = S_2 = 2d$.

Figure 2 shows the schematic diagram of the numerical calculation model. This numerical simulation is based on a two-dimensional rectangular model with dimensions of $H = L = 10d = 381$ mm.

Figure 2 gives the corresponding boundary conditions: 1) A symmetric boundary condition is set on the top and bottom sides of the computational domain. 2) The outlet on the right side of the computational domain is set as a perfectly matched layer (PML) with a certain thickness, so the sound wave is completely absorbed when it propagates here. The thickness of the PML is set to 1/2 the wavelength of the sound wave. 3) Non-slip boundaries are set on the wall of the cylindrical tube. 4) On the left side of the computational domain, a velocity excitation condition is given in the following form:

$$u_\theta = U_0 \sin(2\pi ft), \tag{15}$$

where θ is the direction of sound wave action, U_0 is the acoustic velocity amplitude, f is the excitation frequency, t is the time.

As shown in Table 1, we choose hot air at 1,200°C as the calculation medium. Other physical parameters of air are given by the COMSOL software material library.

By introducing the Strouhal number $\mathrm{Sr} = fH/U_0$, the velocity boundary condition (15) can be transformed into the following dimensionless form:

$$u_\theta^* = \sin(2\pi Sr \cdot \tau). \tag{16}$$

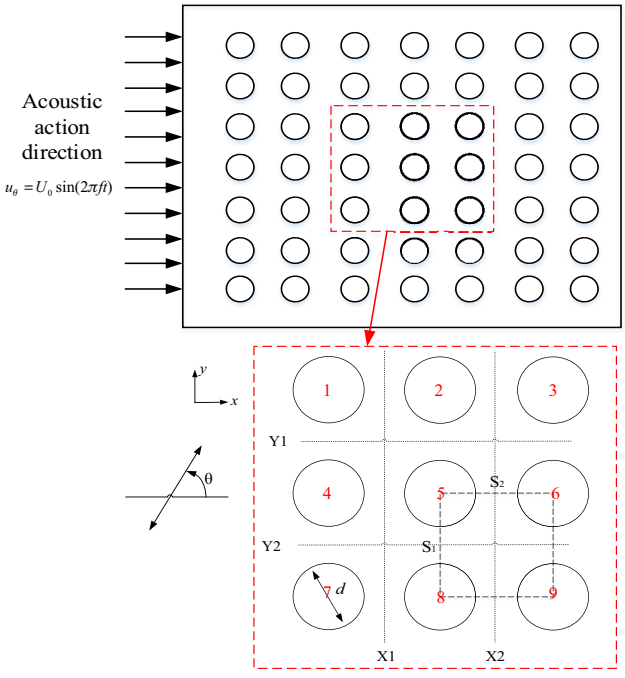

Figure 1: An illustration of the structure of a cylindrical tube array.

3.2 Numerical procedure

Based on multi-physical field software COMSOL 6.2, we use the Reynolds stress method with a separate time scale to solve Eqs. (11) and (12) step by step. The main steps are as follows:

Table 1: Calculation medium parameters

Parameter	Value
Density, ρ_0	0.2395 kg m^{-3}
Sound speed, c_0	745.013 m s^{-1}
Dynamic viscosity, μ	5.5847 × 10^{-5} Pa s
Thermal conductivity, k	0.09 W m^{-1} K^{-1}

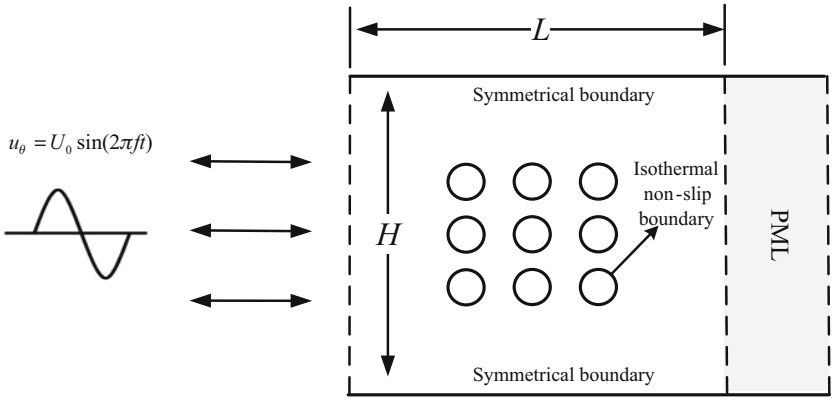

Figure 2: Numerical calculation model of cylindrical tube array.

A pre-defined acoustic module is used to solve the first-order harmonic field formed in the computational domain under the excitation of the boundary condition (16). The solution equation of the first-order sound pressure p_1^* is as follows:

$$L^2 p_1^* + \frac{\omega^2}{c^2} H^2 p_1^* = 0. \tag{17}$$

Eq. (17) is called the dimensionless Helmholtz wave equation. Then, by combining the first-order continuity Eq. (7) and the first-order momentum Eq. (8), the corresponding first-order sound velocity field u_1^* and density field ρ_1^* can be obtained.

The predefined computational fluid dynamics (CFD) laminar flow module is used to solve the acoustic streaming control Eqs. (11) and (12). The first-order harmonic sound field obtained in the first step is used as the source term to solve the second-order acoustic streaming flow field.

The source term to the right of Eqs. (11) and (12) is calculated as follows:

a) The mass source term can be solved by adding a weak contribution in the CFD module of the COMSOL software. The mass source to the right of the equal sign of Eq. (12) has the following expression:

$$\begin{aligned} \text{Mass source} &= -L \cdot \langle \rho_1^* \boldsymbol{u}_1^* \rangle \\ &= -\left(\frac{\partial \langle \rho_1^* u_1^* \rangle}{\partial X} + \frac{\partial \langle \rho_1^* v_1^* \rangle}{\partial Y} \right) \\ &= -\frac{1}{2} \left\{ \frac{\partial \{ \mathrm{Re}[\mathrm{conj}(\rho_1^*) \cdot u_1^*] \}}{\partial X} \right. \\ &\quad \left. + \frac{\partial \{ \mathrm{Re}[\mathrm{conj}(\rho_1^*) \cdot v_1^*] \}}{\partial Y} \right\}. \end{aligned} \tag{18}$$

where u_1^* and v_1^* are the first-order dimensionless velocities in the x- and y-directions, respectively. The operator conj() takes the complex conjugate of the variable. The operator Re[] represents taking the real part of a complex variable. In COMSOL, the weak contribution to Eq. (18) is added as follows:

$$\text{Weak Contribution} = \int_{\Omega} (\text{Mass source} \cdot \tilde{p}_2) \mathrm{d}V. \tag{19}$$

where $\tilde{p}_2$ is the pressure test function.

b) For the volume force term, the finite element software COMSOL can directly add the volume force sub-module to solve the problem. The volume force term on the right of the equal sign of Eq. (11) has the following expression:

In the x-direction:

$$\begin{aligned} F_{Vx} &= \left\langle \rho_1^* \frac{\partial \boldsymbol{u}_1^*}{\partial \tau} \right\rangle + \rho_0^* \langle (\boldsymbol{u}_1^* \cdot L) \boldsymbol{u}_1^* \rangle \\ &= \left\langle \rho_1^* \frac{\partial u_1^*}{\partial \tau} \right\rangle + \rho_0^* \left\langle u_1^* \frac{\partial u_1^*}{\partial X} \right\rangle + \rho_0^* \left\langle v_1^* \frac{\partial u_1^*}{\partial Y} \right\rangle \\ &= \frac{1}{2} \mathrm{Re}[\mathrm{conj}(\rho_1^*) \cdot (-i\omega u_1^*)] \\ &\quad + \frac{1}{2} \rho_0^* \mathrm{Re}\left[\mathrm{conj}(u_1^*) \cdot \frac{\partial u_1^*}{\partial X} \right] \\ &\quad + \frac{1}{2} \rho_0^* \mathrm{Re}\left[\mathrm{conj}(v_1^*) \cdot \frac{\partial u_1^*}{\partial Y} \right]. \end{aligned} \tag{20}$$

In the y-direction:

$$\begin{aligned} F_{Vy} &= \left\langle \rho_1^* \frac{\partial \boldsymbol{u}_1^*}{\partial \tau} \right\rangle + \rho_0^* \langle (\boldsymbol{u}_1^* \cdot L) \boldsymbol{u}_1^* \rangle \\ &= \left\langle \rho_1^* \frac{\partial v_1^*}{\partial \tau} \right\rangle + \rho_0^* \left\langle u_1^* \frac{\partial v_1^*}{\partial X} \right\rangle + \rho_0^* \left\langle v_1^* \frac{\partial v_1^*}{\partial Y} \right\rangle \\ &= \frac{1}{2} \mathrm{Re}[\mathrm{conj}(\rho_1^*) \cdot (-i\omega v_1^*)] \\ &\quad + \frac{1}{2} \rho_0^* \mathrm{Re}\left[\mathrm{conj}(u_1^*) \cdot \frac{\partial v_1^*}{\partial X} \right] \\ &\quad + \frac{1}{2} \rho_0^* \mathrm{Re}\left[\mathrm{conj}(v_1^*) \cdot \frac{\partial v_1^*}{\partial Y} \right]. \end{aligned} \tag{21}$$

To sum up, in the laminar flow module of CFD, Eqs. (18) and (19) are added to the continuity equation by writing codes, and Eqs. (20) and (21) are added to the momentum equation for numerical solution.

3.3 Meshing method

The viscous dissipation of sound waves in the acoustic boundary layer on the wall of the cylindrical tube is the main way to transform the acoustic energy into the kinetic energy of the fluid, and it is also the fundamental reason for generating and driving the acoustic streaming. The thickness of the acoustic boundary layer formed by sound waves on the wall of the cylindrical tube is evaluated by the following formula [29,30]:

$$\delta_v = \sqrt{\frac{2\nu}{\omega_1}} = \sqrt{\frac{H^2}{\pi \mathrm{Sr} \cdot \mathrm{Re}}}, \tag{22}$$

where ν is the kinematic viscosity of the fluid and ω_1 is the excitation angular frequency, $\omega_1 = 2\pi f$.

According to Eq. (22), the thickness of the acoustic boundary layer decreases with the increase in the product

of Strouhal number and acoustic Reynolds number. For example, when acoustic Reynolds number Re = 16.34 and Strouhal number Sr = 200, the thickness of the acoustic boundary layer δ_v = 0.96 mm is calculated from Eq. (22). Therefore, the physical field in the acoustic boundary layer must be solved accurately, which requires that the mesh near the cylindrical wall must be very fine.

Referring to the methods in the study by Nama *et al.* [27] and Lee and Wang [30], the computational domain mesh is generated by setting the maximum element length of the boundary layer region as d_{mesh} and the maximum element length of the main fluid region outside the layer as $20d_{\text{mesh}}$. For given parameters, the mesh density can be adjusted by changing the value of d_{mesh}/δ_v, so as to analyze the sensitivity of the numerical solution to the number of meshes. For the second-order nonlinear acoustic problem, it is reasonable to choose the second-order streaming velocity as the parameter of the stability criterion of the numerical solution. As shown in Figure 3, the variation in time-averaged second-order streaming velocity with the value of d_{mesh}/δ_v is given. The parameters of the example are Re = 163.39 and Sr = 200. From Figure 3, when $d_{\text{mesh}} < 3\delta_v$, the numerical solution is basically stable.

Figure 4 shows the meshing results. In the acoustic boundary layer, a free quadrilateral mesh with the height of the first layer of $\delta_v/10$, the expansion ratio of 1.2, and the number of boundary layers of 10 is generated. In addition, the calculation domain outside the boundary layer is divided by triangular mesh.

3.4 Numerical method verification

In order to verify the reliability of the numerical solution of acoustic streaming by the Reynolds stress method, we try to use this method to calculate the acoustic streaming around a single cylindrical tube. By defining the normalized acoustic streaming velocity U, and comparing the numerical results with the Chun L.P. analytical solution [30] and Nybrog numerical solution [31], the reliability of the numerical method used in this study is verified.

$$U = u_2^*/\max(u_2^*). \tag{23}$$

In the case that the wavelength is greater than the diameter of the cylindrical tube, Chun L.P. gave the analytical solution form of the flow velocity of acoustic streaming outside the boundary layer of the cylindrical tube in the standing wave field in a cylindrical coordinate system.

$$u_{2\theta} = -\frac{3A^2}{2\omega R\rho_0^2 c^2}\left\{\begin{array}{l}\cos^2(kx)\left(\frac{R}{r}\right)^3\sin(2\theta) + \frac{1}{4}(kR)\sin(kx)\cos(kx)\left[1\right.\\ \left.+\left(\frac{R}{r}\right)^2\right]\sin(\theta)\\ +\frac{3}{4}(kR)\sin(kx)\cos(kx)\left[\left(\frac{R}{r}\right)^2 - 3\left(\frac{R}{r}\right)^4\right]\sin(3\theta)\end{array}\right\}, \tag{24}$$

$$v_{2r} = \frac{3A^2}{2\omega R\rho_0^2 c^2}\left\{\begin{array}{l}\cos^2(kx)\left[\frac{R}{r} - \left(\frac{R}{r}\right)^3\right]\cos(2\theta) + \frac{1}{4}(kR)\sin(kx)\cos(kx)\left[1\right.\\ \left.-\left(\frac{R}{r}\right)^2\right]\cos(\theta)\\ -\frac{9}{4}(kR)\sin(kx)\cos(kx)\left[\left(\frac{R}{r}\right)^2 - \left(\frac{R}{r}\right)^4\right]\cos(3\theta)\end{array}\right\}, \tag{25}$$

where $u_{2\theta}$ and v_{2r} is the circumferential and radial second-order acoustic streaming velocity component, respectively; k is the wave number; R is the radius of the cylindrical tube; and x indicates the position of the cylindrical tube. For example, x = 0 indicates that the cylindrical tube is at the sound pressure node, A is the amplitude of the acoustic wave, and θ represents the azimuth of the space around the cylindrical tube. The magnitude of streaming velocity is $u_2^* = \sqrt{u_{2\theta}^2 + v_{2r}^2}$.

Nyborg's numerical solution is to mathematically process the inner streaming vortex in the extremely thin acoustic boundary layer into a slip velocity to predict the acoustic streaming outside the acoustic boundary layer. For the cylindrical tube model, the mathematical expression of the circumferential wall slip velocity has the following form [31]:

$$U_L = -\frac{1}{4\omega}\,\text{Re}\left\{u_{1\tau}\frac{\mathrm{d}u_{1\tau}^*}{\mathrm{d}\tau} + u_{1\tau}^*\left[(2+i)\left(\frac{\mathrm{d}u_{1\tau}}{\mathrm{d}\tau} + \frac{\mathrm{d}w_{1n}}{\mathrm{d}n}\right) - (2+3i)\frac{\mathrm{d}w_{1n}}{\mathrm{d}n}\right]\right\}, \tag{26}$$

where $u_{1\tau}$ and w_{1n} are tangential and normal components of first-order acoustic velocity, respectively. For specific physical meanings of other variables in Eq. (26), please

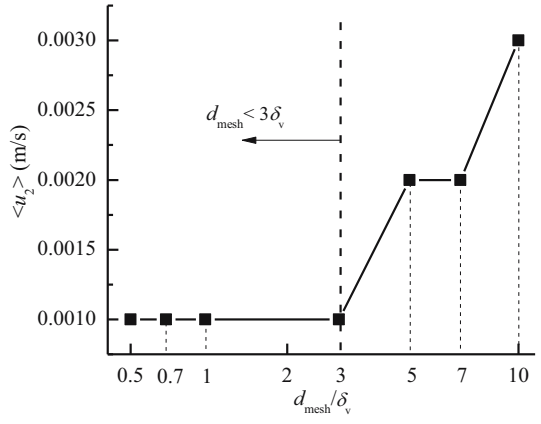

Figure 3: Mesh convergence analysis.

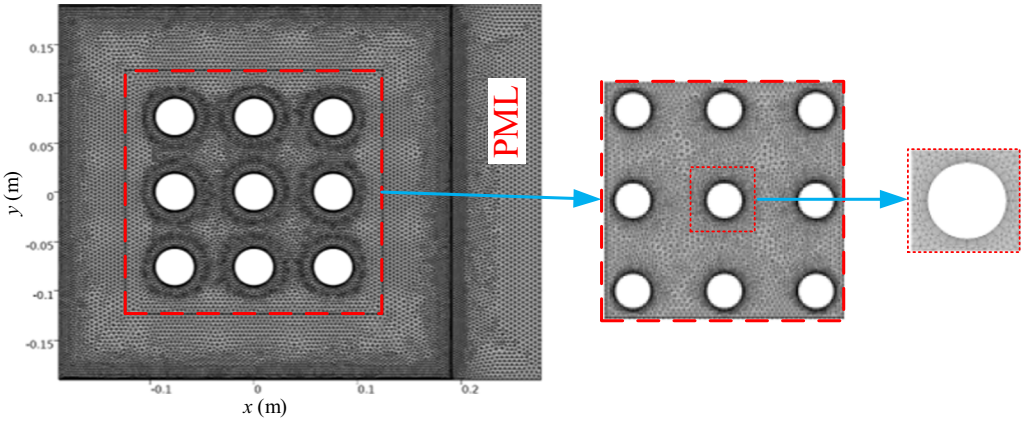

Figure 4: Local meshing results of the computational domain.

refer to the study by Lei *et al.* [31]. The method of numerical calculation through Eq. (26) is also known as the limit slip velocity method [28], which is only applicable when the radius of curvature on the surface of the cylindrical tube is greater than the thickness of the acoustic boundary layer.

The given calculation parameters are velocity amplitude $U_0 = 0.01\ \mathrm{m\ s^{-1}}$ and acoustic frequency $f = 1{,}000$ Hz. As shown in Figure 5(a), when the cylindrical tube is at the sound pressure nodal position, the four outer streaming vortices around the cylinder are symmetrically distributed in relation to the x and y axes, respectively. Figure 5(b) gives the comparison of normalized streaming velocities with normal directions of 0° and 45° outside a single cylindrical tube.

From Figure 5(b), the numerical results in this study are consistent with the overall variation trend of Chun P.L. analytical solution and Nyborg numerical solution. The results obtained by the numerical method used in this study are in good agreement with Nyborg's numerical solution. This shows that the Reynolds stress method is suitable for the simulation of acoustic streaming outside a cylindrical tube. Besides, the error between the numerical solution and the Chun P.L. analytical solution increases with the increase in r, because the analytical solution of Chun P.L. is obtained under the assumption that the computation domain is infinite, and there is a truncation error.

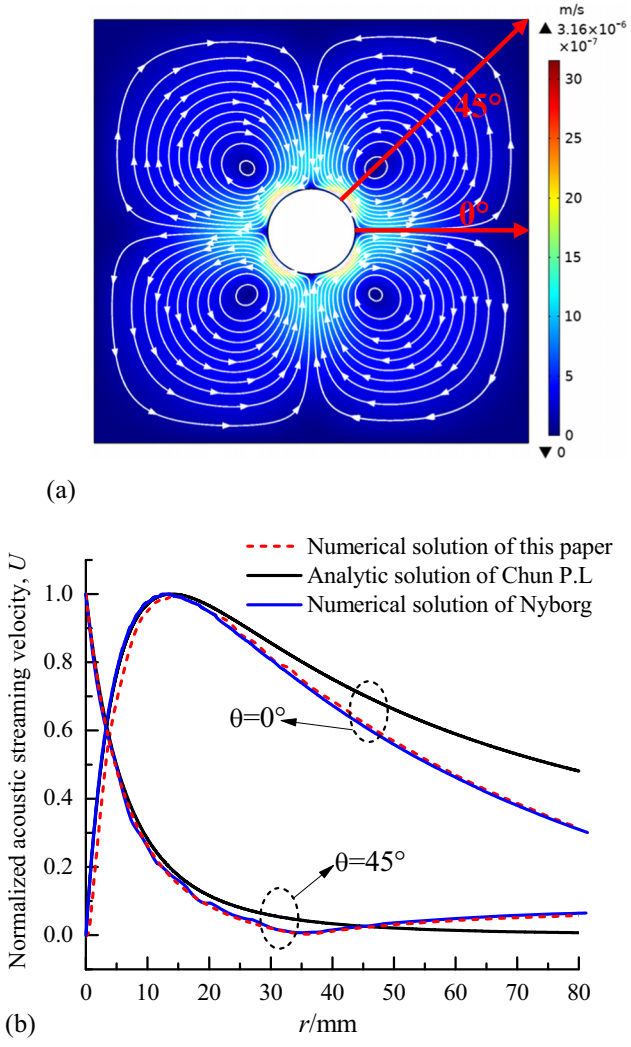

Figure 5: Verification of numerical results. (a) The acoustic streaming around the cylindrical tube. (b) Comparison of numerical results.

4 Results and discussion

Table 2 shows the dimensionless parameters selected in this work and the corresponding acoustic parameter values.

Table 2: Dimensionless parameters and corresponding acoustic parameter values

Serial number	Acoustic Reynolds number Re	Strouhal number Sr	Acoustic frequency f (Hz)	Sound pressure level SPL (dB)	Particle velocity amplitude U_0 (m s^{-1})
1	16.3	100	2.62	103.33	0.01
2	32.7	100	5.25	109.33	0.02
3	49.0	50	3.94	112.85	0.03
4	49.0	100	7.87	112.85	0.03
5	49.0	200	15.75	112.85	0.03
6	49.0	300	23.62	112.85	0.03
7	49.0	1,000	78.74	112.85	0.03
8	49.0	2,000	157.48	112.85	0.03
9	130.7	100	21.00	121.37	0.08
10	245.05	100	39.37	124.17	0.15
11	326.78	100	52.49	129.33	0.2
12	490.18	100	78.74	132.85	0.3
13	653.57	100	404.99	135.35	0.4
14	817.0	100	131.23	137.29	0.5
15	1633.9	100	262.47	143.31	1
16	1633.9	200	524.93	143.31	1

From Table 2, the sound frequencies corresponding to the dimensionless parameters are mainly concentrated in the low-frequency range (2.62–524.93 Hz). This is because low-frequency sound waves have strong penetrability in the tube array, and the sound energy attenuation is weak. Therefore, the selection of low-frequency sound waves is beneficial to effectively enhance heat transfer and sonic cleaning in most areas of the tube array. The sound pressure level corresponding to the dimensionless parameters covers the continuous variation from low sound pressure level to high sound pressure level (103.33–143.31 dB), which is helpful in investigating the influence of sound field intensity on the evolution of the acoustic streaming.

4.1 Acoustic streaming in tube array at different acoustic incident angles

When the acoustic Reynolds number Re = 1633.9 and Strouhal number Sr = 200, Figure 6 shows the influence of different incident angles (θ = 0°, 15°, 30°, and 45°) on the acoustic streaming in the tube array structure. For a given dimensionless parameter, the thickness of the acoustic boundary layer is δ_v = 0.38 mm. Under this parameter, the internal vortex scale in the acoustic boundary layer is very small. Therefore, Figure 5 shows only the vortex structure outside the acoustic boundary layer.

From Figure 6, the acoustic streaming in the tube array presents a variety of flow field structures under different acoustic incidence angles. When the acoustic incident angle θ = 0°, four acoustic streaming vortice structures are evenly distributed around the cylindrical tube, and any two adjacent vortice structures always counter-rotate. With the change in acoustic incident angle, when θ = 15° and θ = 30°, the adjacent vortex structures interact with each other, and two vortex structures gradually appear in the phenomenon of mergers. When θ = 45°, the two vortex structures gradually merge into one large vortex structure. In addition, there are four strong airflows around each cylindrical tube wall. From Figure 6, the maximum streaming velocity only appears on the walls of each cylindrical tube, and its velocity reaches 30 mm s^{-1}. Under the action of sound waves, the wall of the cylindrical tube is always affected by the four external vortices of strong acoustic streaming, and the position of the vortex changes with the change in the acoustic incidence angle. This strong acoustic streaming vortex on the wall plays an important role in destroying the thickness of the boundary layer and provides a physical explanation for the interaction mechanism between sound waves and cylindrical tubes.

To further explain the influence of the acoustic incident angle on the acoustic streaming in the tube array structure, Figure 7 shows the variation curve of acoustic streaming velocity U_2 on the centerline (X1) between the first column and the second column of tubes in the tube array with the acoustic incidence angle.

From Figure 7, the acoustic incident angle has little effect on the acoustic streaming velocity distribution between the tubes. Combined with Figure 6, it can be seen that the difference in the acoustic streaming velocity distribution is caused by the change in the flow field structure in the tube array. In Figure 7, there are six maximum and five minimum values of streaming velocity in the streaming velocity distribution.

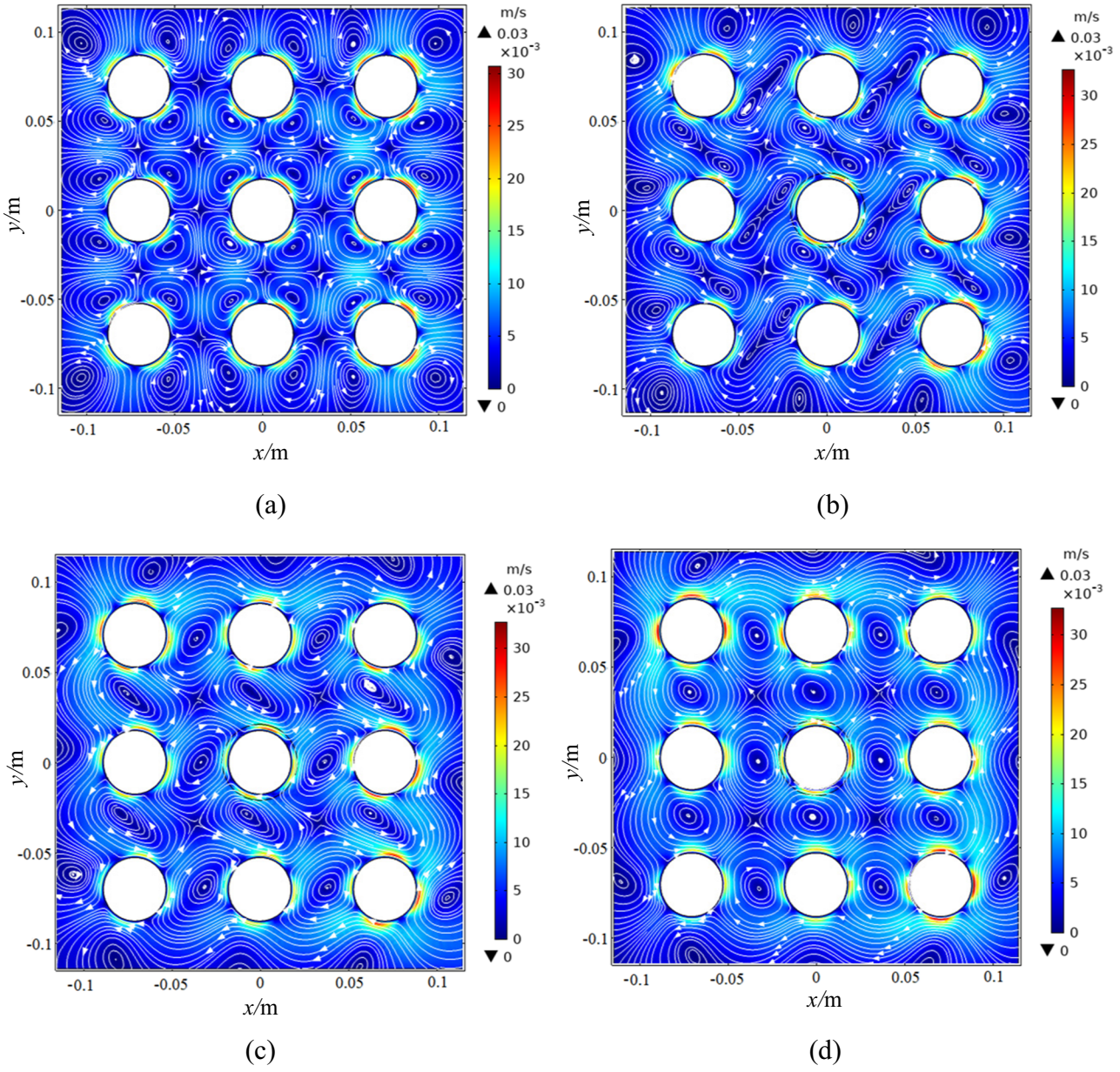

Figure 6: Influence of acoustic incident angles on the acoustic streaming structure: Sr = 200 and Re = 1633.9. (a) θ = 0°. (b) θ = 15°. (c) θ = 30°. (d) θ = 45°.

The position of the maximum streaming velocity is just near the interface of the two adjacent vortices because the adjacent vortices have the same velocity direction at the interface. The minimum streaming velocity appears near the center of the vortex because there is no airflow in the center of the vortex.

Figure 8 gives the acoustic streaming flow velocity on the circumference near the wall of the central cylindrical tube at different incident angles, and the circumference radius is $r = R + 10\delta_v$.

In Figure 8, the peak value of the acoustic streaming velocity near the central tube changes with the change in the acoustic incidence angle. The streaming velocity distribution curve is zigzag, which is caused by the distortion of the flow field caused by the interaction between the acoustic streaming vortices in the tube array. From Figure 8(a), when the acoustic incident angle is 0°, four streaming velocity peaks appear around the central cylindrical tube, which is sequentially distributed in the azimuths of 45°, 135°, 225°, and 315°. This is because the positions of the four strong acoustic streaming vortices near the wall of the tube change with the change in the acoustic incident angle, which can be clearly seen in Figure 6. Therefore, the peak position of

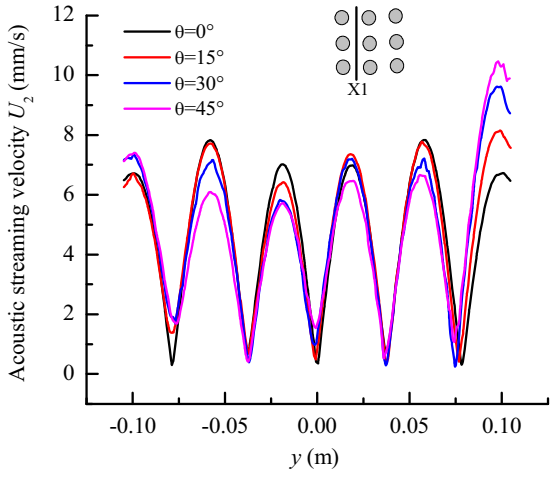

Figure 7: Comparison of acoustic streaming velocity between tubes at different acoustic incidence angles: Sr = 200 and Re = 1633.9.

acoustic streaming velocity changes with the change in acoustic incident angle. In Figure 7(b), when the acoustic incident angle is 15°, the streaming velocity peaks are sequentially distributed in the azimuths of 60°, 150°, 240°, and 330°. In Figure 8(c), when the acoustic incident angle is 30°, the streaming velocity peaks are sequentially distributed in the azimuths of 75°, 165°, 255°, and 345°. In Figure 8(d), when the acoustic incidence angle is 45°, the streaming velocity peaks are sequentially distributed in the azimuths of 90°, 180°, 270°, and 360°. Therefore, from the perspective of heat transfer enhancement, the effect of acoustic streaming on the local convective heat transfer around the cylindrical tube is closely related to the incident angle of the acoustic wave. In summary, when the incident angle is θ, the positions of the four acoustic streaming vortices around the cylindrical tube are in the azimuth of 45° + θ, 135° + θ, 225° + θ, and 315° + θ, respectively.

4.2 Acoustic streaming in tube array under different acoustic Reynolds number

For Strouhal number Sr = 100, Figure 9 presents the flow field characteristics of acoustic streaming in the tube array at different acoustic Reynolds numbers (Re = 16.3, 32.7, 49.0, 130.7, 817.0, and 1633.9).

From the definition of acoustic Reynolds number (Re = U_0H/ν), we know that dimensionless acoustic Reynolds number determines the relative strength of the inertia effect and viscous effect. The greater the acoustic Reynolds number, the greater the fluid inertia effect caused by sound waves. The smaller the acoustic Reynolds number is, the stronger the viscous dissipation effect is.

As can be seen from Figure 9, in the structural field of a cylindrical tube array, the acoustic streaming vortex presents different flow field characteristics with the increase in acoustic Reynolds number, which is embodied in the shrinking and splitting of the acoustic streaming vortex and the enhancement of flow field intensity. As shown in Figure 9(d), a large vortex structure between adjacent cylindrical tubes is split into two small-scale vortex structures and a larger-scale vortex structure. From Eq. (17), the viscous dissipation scale of sound waves around the cylindrical tube is inversely proportional to the acoustic Reynolds number. Therefore, when the acoustic Reynolds number is small, such as Re = 16.3, the viscous dissipation scale of the sound wave on the cylindrical tube wall is equivalent to the tube spacing. At this time, two adjacent internal vortices merge into a larger-scale vortex structure, as shown in Figure 9(a). With the increase in the acoustic Reynolds number, the penetration distance of the viscous dissipation of the sound wave on the wall of the cylindrical tube decreases, which leads to the decrease in the inner vortices size of the acoustic streaming in the acoustic boundary layer. It can be seen from Figure 9(b) and (c) that the large vortex structure between adjacent tubes gradually splits as the acoustic Reynolds number increases. It should be noted that in Figure 9(a)–(c), due to the small Strouhal number and acoustic Reynolds number selected, the significant viscous dissipation of sound waves on the wall of the cylindrical tube can form a thicker acoustic boundary layer. At this time, the vortex structure present in the tube array is all inner streaming vortices, as shown in Figure 9(a). When the acoustic Reynolds number is large, such as Re = 130.7, the inertial effect of the sound wave-induced oscillating flow is much greater than the viscous effect. At this time, the viscous penetration distance of the sound wave on the cylindrical tube wall is extremely small. In Figure 9(d), it can be seen that there are four extremely small-scale vortex structures around the cylindrical tube and a large-scale vortex structure with a counter-rotating appearance outside each small vortex. When the acoustic Reynolds number further increases, as shown in Figure 9(e) and (f), the inner streaming structure disappears and only the outer streaming structure appears. At the same time, the higher the acoustic Reynolds number, the higher the acoustic streaming flow velocity in the tube array. For example, when Re = 1633.9, the maximum streaming velocity can reach 50 mm s^{-1}.

From the above analysis, it can be seen that the main mechanism of acoustic Reynolds number affecting acoustic streaming flow characteristics is determined by the relative size between adjacent tube spacing and acoustic boundary layer thickness. When the thickness of the acoustic boundary

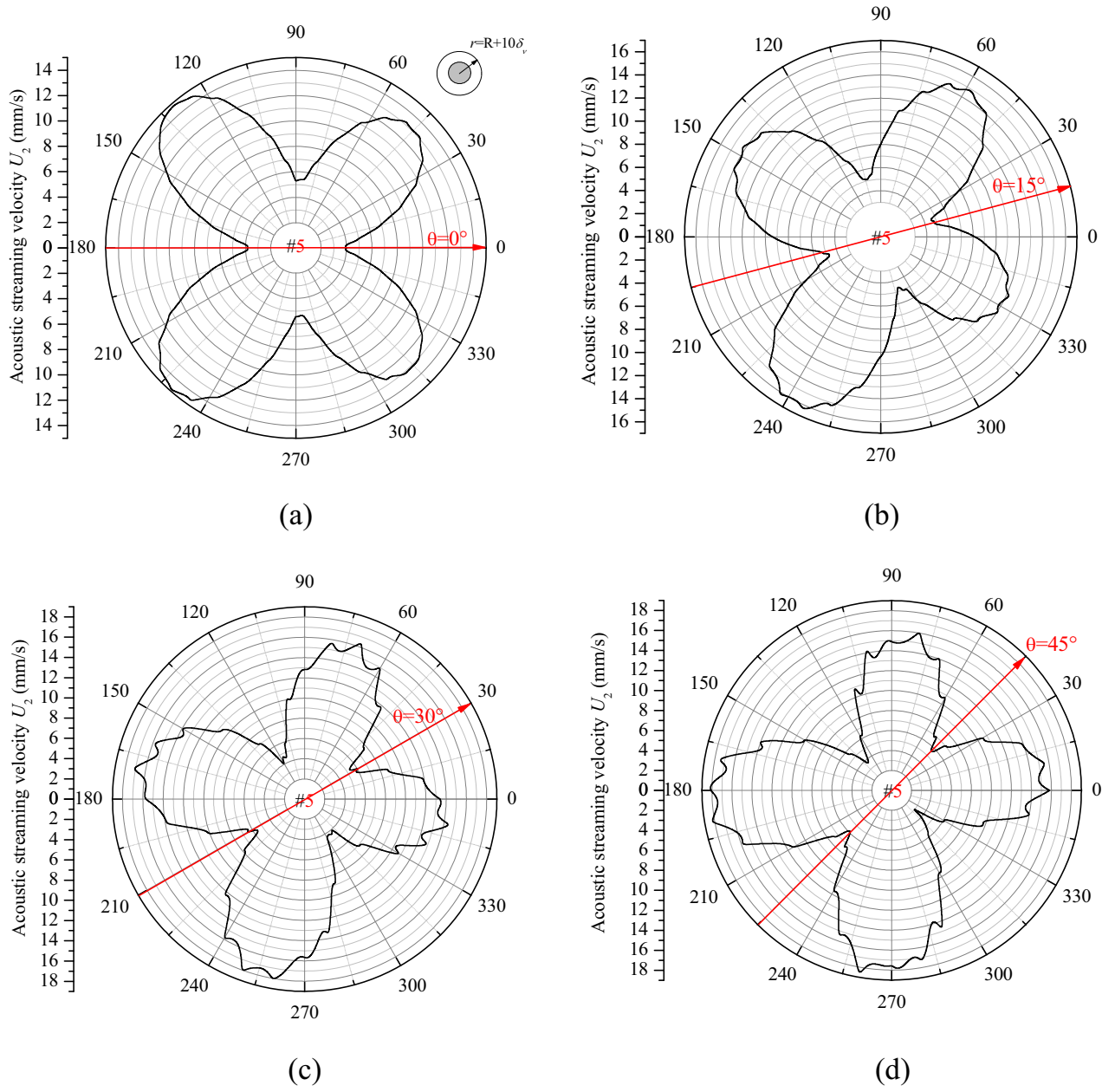

Figure 8: Acoustic streaming flow velocity around the central tube under different acoustic incident angles: Sr = 200 and Re = 1633.9. (a) θ = 0°. (b) θ = 15°. (c) θ = 30°. (d) θ = 45°.

layer is much smaller than the gap scale between the cylindrical tubes, only the vortices outside the boundary layer appear in the tube array. When the thickness of the acoustic boundary layer is larger than the gap scale between the cylindrical tubes, only the vortices in the boundary layer are shown.

Figure 10 gives the variation in the maximum streaming velocity $U_{2\max}$ with acoustic Reynolds number in the tube array.

From Figure 10, when Re < 100, the acoustic streaming intensity is very weak. When Re > 100, the acoustic streaming intensity increases rapidly. Within the range of acoustic Reynolds number studied, the following relationship is obtained by fitting the data in Figure 10.

$$U_{2\ \max} = -42.352 + 41.933e^{4.833\times10^{-4}\,\mathrm{Re}}. \tag{27}$$

The correlation coefficient of the fitting formula (27) is 0.999, which describes the nonlinear relationship between the flow intensity of acoustic streaming and the change in acoustic Reynolds number.

According to the definition of sound field intensity, the relationship is as follows:

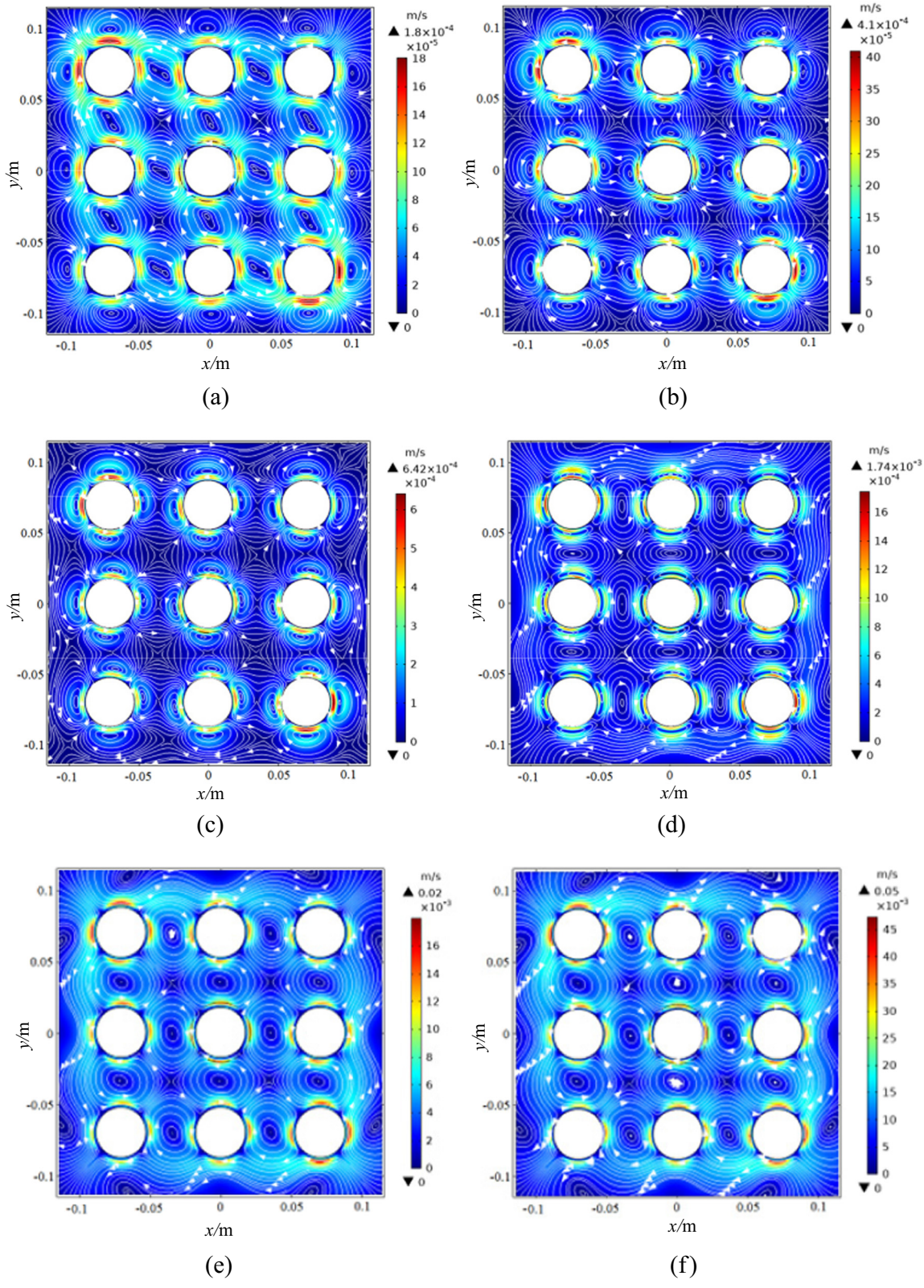

Figure 9: Comparison of acoustic streaming structure in tube array under different acoustic Reynolds number: Sr = 100 and θ = 45°. (a) Re = 16.3. (b) Re = 32.7. (c) Re = 49.0. (d) Re = 130.7. (e) Re = 817.0. (f) Re = 1633.9.

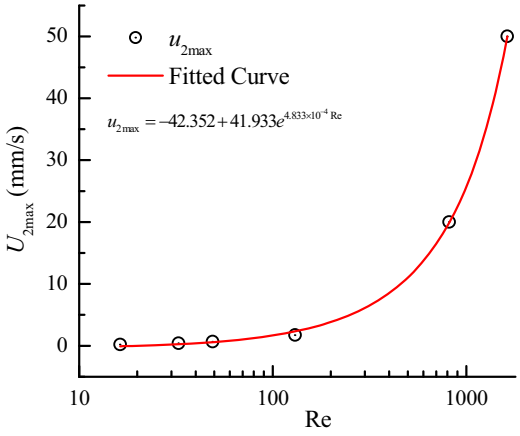

Figure 10: Variation law of maximum streaming velocity with acoustic Reynolds number: Sr = 100 and θ = 45°.

$$\mathrm{SPL} = 20\log_{10}\left(\frac{U_0}{\sqrt{2}\,U_{\mathrm{ref}}}\right) = 20\log_{10}\left(\frac{\nu\,\mathrm{Re}}{\sqrt{2}\,HU_{\mathrm{ref}}}\right). \quad (28)$$

where U_{ref} is the reference vibration velocity of fluid particles, $U_{\mathrm{ref}} = 4.83 \times 10^{-8}\,\mathrm{m\,s^{-1}}$. From Eq. (28), sound field intensity increases logarithmically with the increase in acoustic Reynolds number. Therefore, when the acoustic Reynolds number is small, that is, the sound wave has a lower sound energy, and the sound wave will form a weak acoustic streaming effect. In the case of large acoustic Reynolds number, the strong interaction between the sound wave and the cylindrical tube will form a strong acoustic streaming effect.

Figure 11 shows the comparison curve of acoustic streaming velocity at different acoustic Reynolds numbers on the centerline (X1) between the first column and the second column of cylindrical tubes in the tube array.

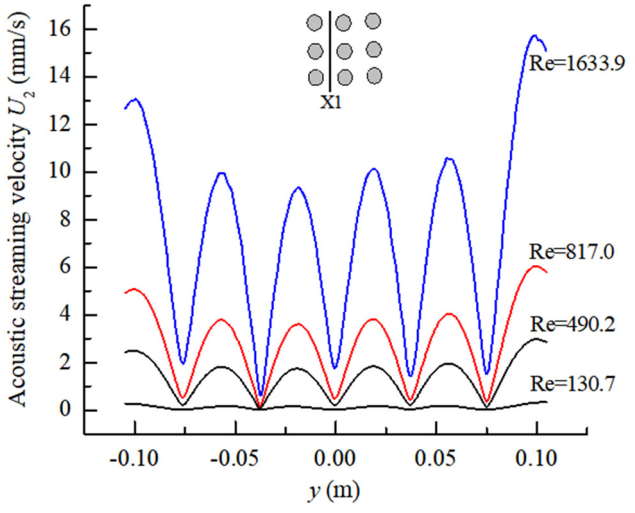

Figure 11: Influence of acoustic Reynolds number on the streaming velocity between the tubes: Sr = 100 and θ = 45°.

From Figure 11, there are six velocity peaks in the acoustic streaming velocity distribution on section line X1. Comparing the analysis with Figure 9, it can be seen that the peak position of the acoustic streaming velocity is just near the interface of the adjacent acoustic streaming vortices, which is consistent with the law shown in Figure 7. The larger the acoustic Reynolds number, the greater the acoustic streaming velocity of the tube array gap. This is because the acoustic streaming structure in the tube array has developed steadily in the range of acoustic Reynolds number Re > 100 (as shown in Figure 9), and further increasing the acoustic Reynolds number will enhance the vortex intensity of the acoustic streaming in the tube array as a whole.

Figure 12 gives the distribution of the acoustic streaming velocity on the circumference of the cylindrical tube near the center of the tube array with different acoustic Reynolds numbers.

In Figure 12, four acoustic flow velocity peaks correspond exactly to the position of the acoustic vortex around the cylindrical tube. From Figure 12, the acoustic streaming velocity around the central cylindrical tube increases as the acoustic Reynolds number increases. For example, the acoustic streaming velocity induced by Re = 1633.9 is 250 times larger than that induced by Re = 16.3. It can be seen that sound waves with a high acoustic Reynolds number (*i.e.*, increasing the sound energy) can significantly enhance the fluid disturbance around the cylindrical tube.

4.3 Acoustic streaming in tube array under different Strouhal number

In the case of acoustic Reynolds number Re = 49 and acoustic incidence angle θ = 45°, Figure 13 shows the acoustic streaming structure in the tube array at different Strouhal numbers Sr = 50, 100, 200, 300, 1,000, and 2,000.

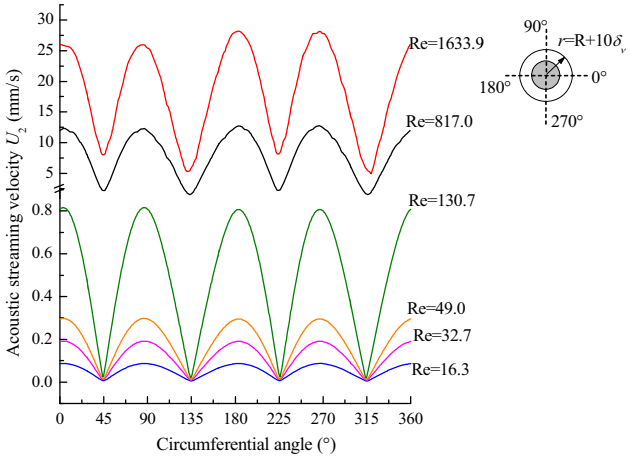

Figure 12: Comparison of streaming velocity around the central cylindrical tube at different acoustic Reynolds number: Sr = 100 and θ = 45°.

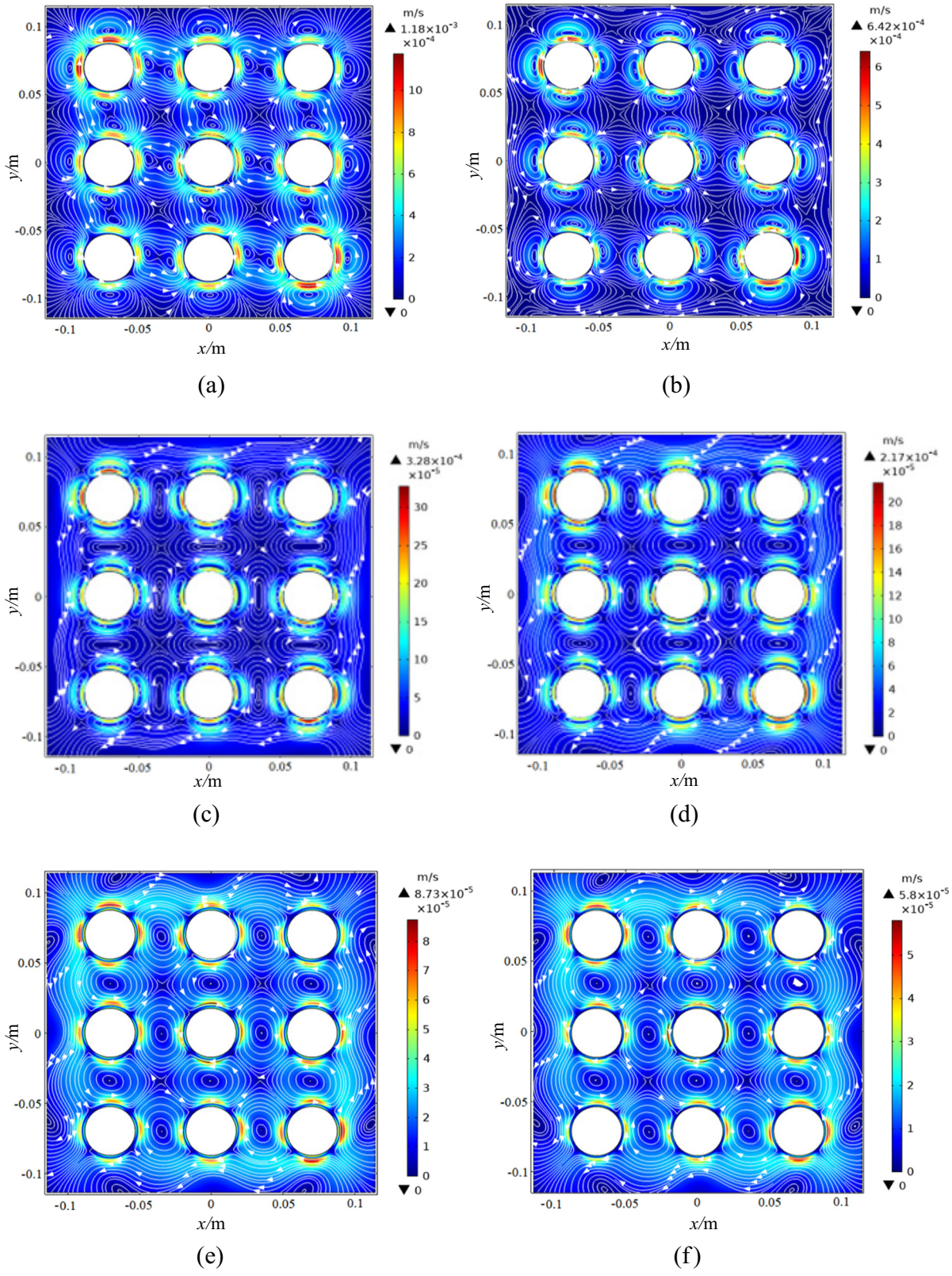

Figure 13: Comparison of acoustic streaming structure in tube array under different Strouhal number: Re = 49 and θ = 45°. (a) Sr = 50. (b) Sr = 100. (c) Sr = 200. (d) Sr = 300. (e) Sr = 1,000. (f) Sr = 2,000.

It can be seen from Figure 13 that the Strouhal number and the acoustic Reynolds number have similar influence rules on the acoustic streaming flow field distribution in the tube array, but their influence mechanisms are different. The sound wave with a smaller Strouhal number has a larger viscous dissipation region on the cylindrical tube wall. On the contrary, the greater the Strouhal number, the smaller the region of viscous dissipation. Therefore, the size of the viscous dissipation region of sound waves on the tube wall determines the structural scale of the acoustic streaming vortex in the acoustic boundary layer. As shown in Figure 13(a) and (b), the smaller Strouhal number (Sr = 50 and Sr = 100) presents a merged acoustic streaming vortices structure in the tube arrays. With the increase in Strouhal number, the large vortices structure undergoes a process of splitting and shrinking in Figure 13(a) and (b). As shown in Figure 13(c) and (d), it results in the vortice structure around the cylindrical tube gradually shrinking close to the wall of the cylindrical tube. With the further increase in Strouhals number, the large vortex structure in Figure 13(a) and (b) splits into two small vortex structures and a relatively large vortex structure. From Figure 13(e) and (f), when the Strouhal number is large, the four small-scale internal vortex structures around each cylindrical tube have disappeared and have been replaced by four large-scale external vortex structures. Also, it can be seen from Figure 13 that the acoustic streaming intensity in the tube array decreases rapidly with the increase in Strouhal number.

In addition, when the acoustic Reynolds number Re = 49, the acoustic streaming velocity is small in the range of the Strouhal number studied in Figure 13. For example, the maximum acoustic streaming velocity corresponding to Sr = 50 is only 1.18 mm s^{-1}. The analysis shows that the sound wave with a low acoustic Reynolds number has a weak interaction with the tube array, resulting in a small velocity of acoustic streaming. However, the velocity of acoustic streaming increases rapidly as the acoustic Reynolds number increases. From Figure 9(f), the maximum value of the acoustic streaming velocity corresponding to Re = 1633.9 and Sr = 100 reaches 50 mm s^{-1}, which is about 78 times higher than the acoustic streaming velocity corresponding to Re = 49.0 and Sr = 100.

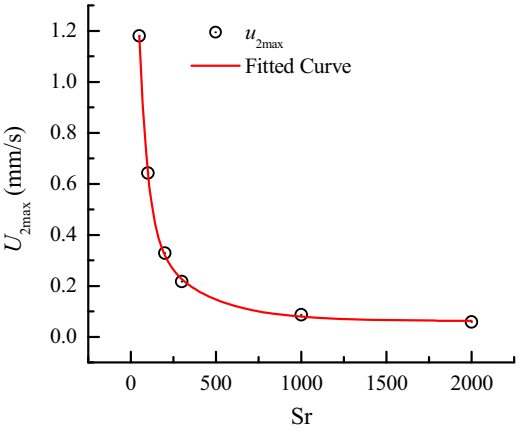

Figure 14: Variation law of the maximum streaming velocity with Strouhal number: Re = 49 and θ = 45°.

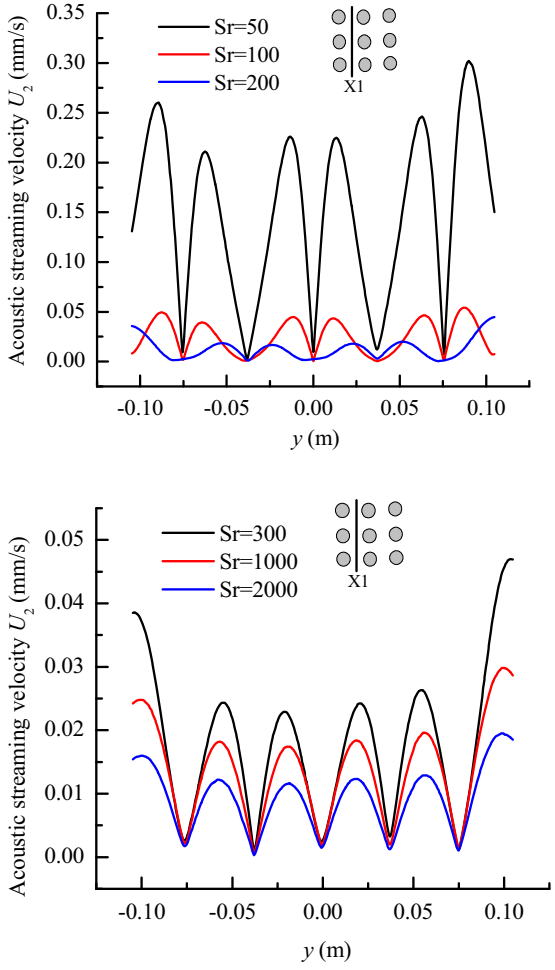

Figure 15: Comparative analysis of acoustic streaming velocity between tubes with different Strouhal numbers: Re = 49 and θ = 45°.

Figure 14 shows the variation in the maximum acoustic streaming velocity U_{2max} with the Strouhal number Sr.

It can be seen from Figure 14 that the maximum acoustic streaming velocity decreases exponentially with the increase in Strouhal number. The acoustic streaming intensity is very sensitive to changes in the small Strouhal number, but it is more stable to changes in the large Strouhal number. Within the range of Strouhal number studied, the following relationship is obtained by fitting the data in Figure 14,

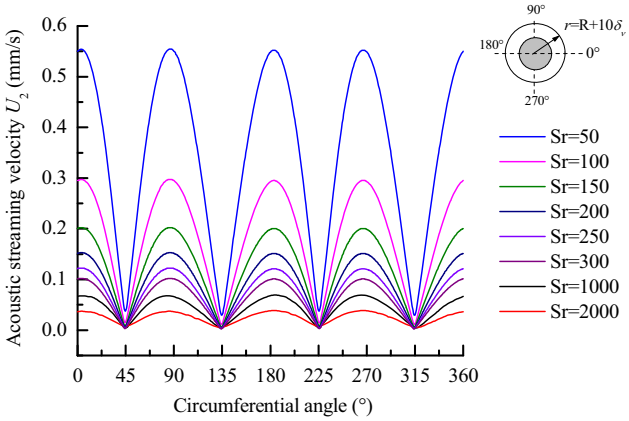

Figure 16: Comparison of streaming velocity around the central cylindrical tube at different Strouhal number: Re = 49 and θ = 45°.

$$U_{2\ \max} = -0.0625 + 2.0728e^{-\mathrm{Sr}/50.1112} + 0.4138e^{-\mathrm{Sr}/312.7256}. \quad (29)$$

The correlation coefficient of the fitting formula (29) is 0.999, which can well describe the nonlinear dependence of the acoustic streaming intensity on the wall of the cylindrical tube on the Strouhal number.

Similarly, to investigate the influence of different Strouhal numbers on the intensity of acoustic streaming in tube array structure field, Figure 15 shows the variation curve of acoustic streaming velocity with the Strouhal numbers on the centerline (X1) between the first column and the second column of cylindrical tubes in the tube array.

From Figure 15, the acoustic streaming velocity between the tubes decreases as the Strouhal number increases. This is because the viscous dissipation effect in the tube array structure field increases with the decrease in the Strouhal number, so the sound energy dissipation caused by the low Strouhal number is larger, which makes the acoustic streaming obtain more energy. The more energy the acoustic streaming obtains, the greater the velocity of acoustic streaming. This also means that a lower Strouhal number can form a stronger acoustic streaming motion.

Figure 16 gives the circumferential acoustic streaming velocity distribution near the cylindrical tube in the center of the tube array with different Strouhal numbers.

From Figure 16, the greater the Strouhal number, the smaller the velocity of acoustic streaming around the central cylindrical tube. Therefore, in order to enhance the thermal convection process of the cylindrical tube and improve the ash removal efficiency, the selected sound source should have a lower Strouhal number. Besides, from the distribution of the acoustic streaming velocity, the flow field disturbance caused by the streaming is not uniform.

From the above analysis, the sound waves with high acoustic Reynolds numbers and low Strouhal numbers can form strong acoustic streaming vortices in the tube array structure field. The acoustic streaming vortex structure around the cylindrical tube is helpful in enhancing the heat transfer. Also, the rich vortex structure in the tube array can greatly enhance the fluid disturbance.

4.4 Details of the acoustic streaming flow field distribution around the central tube of the tube array

In order to clearly present the acoustic streaming field structure around a single cylindrical tube in the tube array, the flow field distribution around the central tube under different acoustic parameters is shown in Figure 16.

In Figure 17(a), the small vortex structure in the acoustic boundary layer and the large vortex structure outside the layer are presented around the cylindrical tube. The position and distribution of the inner vortex structure and the corresponding external vortex structure changes with the change in the acoustic incident angle, and the structure of the external vortex flow field changes greatly. With the increase in the acoustic incident angle, the two external vortex structures connected by the red lines in the picture gradually merge into a new vortex structure with a larger scale.

In Figure 17(b), only the internal eddy current appears around the cylindrical tube. This is because the given acoustic Reynolds number and Strouhal number are very small, the viscous dissipation scale of sound waves on the wall surface of the cylindrical tube is larger than the distance between the cylindrical tubes, so the scale of the internal vortex structure generated is larger than the distance between the tubes. With the increase in the acoustic incident angle, the two internal vortex structures connected by the red lines in the picture gradually merge into a new vortex structure with a larger scale, and the vortex structure develops from the flat type to the expansive type. When the incident angle of sound increases from 0° to 15°, the outer streamline of the two inner vortices connected by the red line in the picture first merges. When the incident angle increases from 15° to 30°, the two internal vortex structures have been completely merged.

In Figure 17(c), the splitting process of the large-scale internal vortex structure around the cylindrical tube is described with the increase in the acoustic Reynolds number. With the increase in the acoustic Reynolds number, the four internal vortex structures around each cylindrical tube gradually contract to the tube wall and finally become a small-

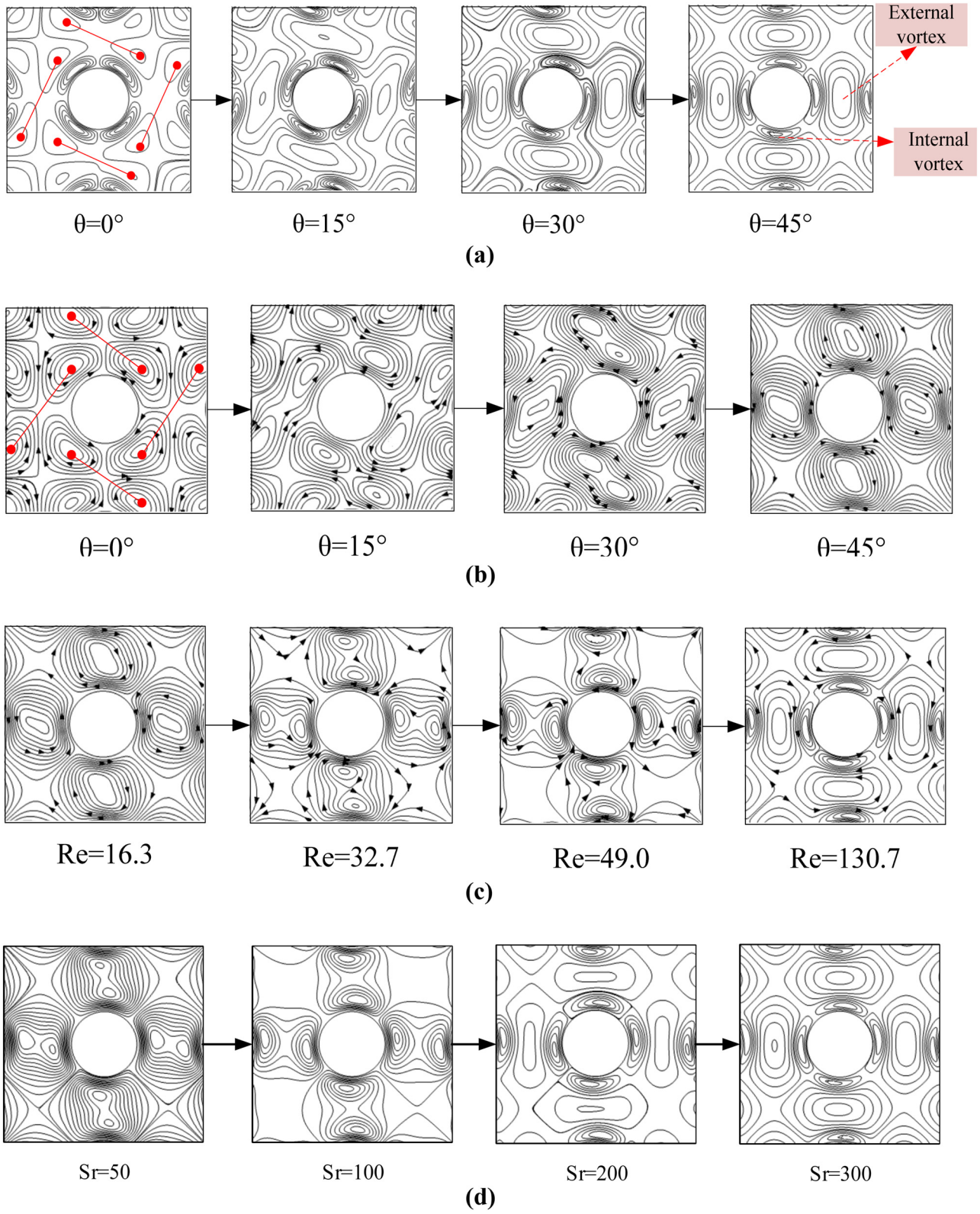

Figure 17: Influence of different acoustic parameters on acoustic streaming field around central tube. (a) Influence of acoustic incident angles on acoustic streaming vortex around the central tube: Sr = 300 and Re = 49.0. (b) Influence of acoustic incident angles on acoustic streaming vortex around the central tube: Sr = 100 and Re = 16.3. (c) Influence of acoustic Reynolds number on acoustic streaming vortex around central tube: Sr = 100 and θ = 45°. (d) Influence of Strouhal number on acoustic streaming vortex around central tube: Re = 49 and θ = 45°.

scale internal vortex structure attached to the tube wall, and the outer vortex structure gradually appears.

In Figure 17(d), the splitting process of the large-scale internal vortex structure around the cylindrical tube is described with the increase in Strouhal number. This process is consistent with the phenomenon described in Figure 17(c). Both the Strouhal number and acoustic Reynolds number are inversely proportional to the thickness of the acoustic boundary layer. Therefore, with the increase in Strouhal number, the viscous dissipation scale of sound waves on the wall of the cylindrical tube decreases rapidly, resulting in the internal vortex structure shrinking and splitting.

To sum up, the acoustic incident angle changes the position of the interaction between the incident wave and the wall of the cylindrical tube, which leads to the change in the position of the acoustic streaming vortex, and the merge occurs when the two vortices with opposite rotating directions meet. The Reynolds number and Strouhal number together determine the thickness of the acoustic viscous boundary layer formed by the plane incident wave on the cylindrical wall of the tube array, which also determines the scale of the inner and outer vortices of the acoustic streaming. Because the viscous dissipation of sound waves on the wall of a cylindrical tube is the physical mechanism of the motion of uniform acoustic streaming driven by periodic sound waves, the sound waves with different combinations of Reynolds number and Strouhal number parameters have rich forms of acoustic streaming motion.

5 Conclusion

In this study, the characteristics of time-averaged acoustic streaming in a cylindrical tube array under the action of sound waves are studied numerically, and the effects of acoustic incident angle, acoustic Reynolds number, and Strouhal number on the acoustic streaming flow field in the tube array are investigated in detail. The main conclusions can be summarized as follows:

1) Sound waves with different incident angles, acoustic Reynolds numbers, and Strouhal numbers can induce rich acoustic streaming fields in the tube array, such as the shrinking, merging, tearing, and splitting of acoustic streaming vortices. With the increase in the acoustic Reynolds number and Strouhal number, the velocity of acoustic streaming increases and decreases exponentially, respectively. The acoustic incidence angle has little effect on the flow velocity in the tube array.
2) When the thickness of the acoustic boundary layer near the wall of the cylindrical tube is much smaller than the gap scale between the cylindrical tubes, only the outer streaming vortices are in the tube array. When the thickness of the acoustic boundary layer is larger than the gap scale between the cylindrical tubes, only the inner streaming vortices are shown.
3) Sound waves with a high acoustic Reynolds number and low Strouhal number can form strong and continuous acoustic streaming vortex motion in the tube array. This kind of fluid motion with vortex characteristics helps strengthen the mixing and disturbance of fluid.
4) The maximum velocity of acoustic streaming in the tube array only appears at the interface of two adjacent vortices and on the tube wall, and there are four maximum velocity values of acoustic streaming in the circumference of the tube wall. The minimum flow velocity occurs in the center of the vortex.

Acknowledgments: This project is supported by Hebei Key Laboratory of Physics and Energy Technology.

Funding information: This work was supported by the National Natural Science Foundation of China (12304491/52206069), the Natural Science Foundation of Hunan Province (2023JJ40010), the Natural Science Foundation of Changsha City (2023cskj017), and the Hebei Key Laboratory of Physics and Energy Technology (HBKLPET2023_02).

Author contributions: All authors have accepted responsibility for the entire content of this manuscript and approved its submission.

Conflict of interest: The authors state no conflict of interest.

Data availability statement: The data that support the findings of this study are available from the corresponding author upon reasonable request.

References

[1] Zhang W, Jiang G, Sun J, Jiang Y. Simultaneous reconstruction of 3D non-uniform temperature and velocity fields in a furnace using a bidirectional acoustic path separation tracking method. Appl Therm Eng. 2024;236:121768.

[2] Jiang G, Liu Y, Kong Q, Xu W, An L. The sound transmission through tube arrays in power boilers based on phononic crystals theory. Appl Therm Eng. 2016;99:1133–40.

[3] Li J, Hou S, Teng D, Shen G. Experimental research on enhanced heat transfer of double-pipe exchanger with audible acoustic field. Int J Heat Mass Transfer. 2023;201:123565.
[4] Liu Y, Jiang G, Yang Y, Kong Q, Jiang Y. Numerical simulation on acoustic streaming characteristics in boiler tube array. Int J Heat Mass Transfer. 2022;193:122834.
[5] El Ghani N, Miralles S, Botton V, Henry D, Ben Hadid H, Ter-Ovanessian B, et al. Acoustic streaming enhanced mass transfer at a wall. Int J Heat Mass Transfer. 2021;172:121090.
[6] Das PK. Acoustic streaming in second-order fluids. Phys Fluids. 2020;32(12):123103.
[7] Manuel Valverde J. Acoustic streaming in gas-fluidized beds of small particles. Soft Matter. 2013;9(37):8792–814.
[8] Kiani H, Sun D. Numerical modeling of particle to fluid heat transfer during ultrasound assisted immersion cooling. Chem Eng Process. 2016;99:25–32.
[9] Dhanalakshmi NP, Nagarajan R, Sivagaminathan N, Prasad BVSSS. Acoustic enhancement of heat transfer in furnace tubes. Chem Eng Process. 2012;59:36–42.
[10] Hamilton MF, Ilinskii YA, Zabolotskaya EA. Acoustic streaming generated by standing waves in two-dimensional channels of arbitrary width. J Acoust Soc Am. 2003;113(1):153–60.
[11] Aktas MK, Farouk B. Numerical simulation of acoustic streaming generated by finite-amplitude resonant oscillations in an enclosure. J Acoust Soc Am. 2004;116(5):2822–31.
[12] Jiang G, Yang Y, Liu Y, Jiang Y. Acoustic streaming outside spherical particles and parameter analysis of heat transfer enhancement. Eur J Mech B-Fluid. 2021;86:1–14.
[13] Baasch T, Doinikov AA, Dual J. Acoustic streaming outside and inside a fluid particle undergoing monopole and dipole oscillations. Phys Rev E. 2020;101(1):13108.
[14] Nuriev AN, Egorov AG, Zaitseva ON. Numerical analysis of secondary flows around an oscillating cylinder. J Appl Mech Tech Phys. 2018;59(3):451–9.
[15] Bahrani SA, Périnet N, Costalonga M, Royon L, Brunet P. Vortex elongation in outer streaming flows. Exp Fluids. 2020;61(3):1–16.
[16] Riley N. Steady streaming. Annu Rev Fluid Mech. 2001;33:43–65.
[17] Suh YK. Streaming flow induced by two oscillating circular cylinders. J Mech Sci Technol. 1995;9(4):506–14.
[18] Yan B, Ingham DB, Morton BR. Streaming flow induced by an oscillating cascade of circular cylinders. J Fluid Mech. 1993;252:147–71.
[19] Coenen W. Steady streaming around a cylinder pair. Proc R Soc A-Math Phys. 2016;472(2195):20160522.
[20] Valverde JM. Pattern-formation under acoustic driving forces. Contemp Phys. 2015;56(3):338–58.
[21] An H, Liang C, Ming Z. Steady streaming around a circular cylinder in an oscillatory flow. Ocean Eng. 2009;36(14):1089–97.
[22] Chini GP, Malecha Z, Dreeben TD. Large-amplitude acoustic streaming. J Fluid Mech. 2014;744:329–51.
[23] Malecha Z. Three-dimensional numerical study of acoustic streaming phenomenon in rectangular resonator. Fluid Dy Res. 2023;55(1):015504.
[24] Yang Y, Jiang G, Liu Y, Yang Y. Flow field characteristics of Rayleigh streaming in a two-dimensional rectangular channel under the background physical field. Int Commun Heat Mass. 2023;142(12):106643.
[25] Sadhal SS. Acoustofluidics 13: Analysis of acoustic streaming by perturbation methods. Lab Chip. 2012;12(13):2223–92.
[26] Muller PB, Barnkob R, Jensen MJ, Bruus H. A numerical study of microparticle acoustophoresis driven by acoustic radiation forces and streaming-induced drag forces. Lab Chip. 2012;12(22):4617–27.
[27] Nama N, Huang PH, Huang TJ, Costanzo F. Investigation of micromixing by acoustically oscillated sharp-edges. Biomicrofluidics. 2016;10(2):24124.
[28] Lei J, Glynne-Jones P, Hill M. Comparing methods for the modelling of boundary-driven streaming in acoustofluidic devices. Microfluid Nanofluid. 2017;21(2):1–11.
[29] Muller PB, Bruus H. Numerical study of thermoviscous effects in ultrasound-induced acoustic streaming in microchannels. Phys Rev E Stat Nonlinear Soft Matter Phys. 2014;90(4):43016.
[30] Lee CP, Wang TG. Outer acoustic streaming. J Acoust Soc Am. 1990;88(5):2367–75.
[31] Lei J, Cheng F, Li K. Numerical simulation of boundary-driven acoustic streaming in microfluidic channels with circular cross-sections. Micromachines-Basel. 2020;11(3):240.